Hindawi
Advances in Civil Engineering
Volume 2019, Article ID 7108262, 18 pages
https://doi.org/10.1155/2019/7108262

Research Article

Detection and Prediction of Internal Damage in the Ancient Timber Structure Based on Optimal Combined Model

Ziyi Wang,[1,2,3] **Donghui Ma**,[2,3,4] **Wei Qian**,[2,3,4] **Wei Wang**,[2,3,4] **Xiaodong Guo**,[2,3,4] **Qingfeng Xu**,[5] **Junhong Huan**,[1,3] **and Zhongwei Gao**[1,3]

[1]*College of Architecture and Civil Engineering, Beijing University of Technology, Beijing 100124, China*
[2]*Institute of Earthquake Resistance and Disaster Reduction, Beijing University of Technology, Beijing 100124, China*
[3]*Key Science Research Base of Safety Assessment and Disaster Mitigation for Traditional Timber Structure (Beijing University of Technology), State Administration for Cultural Heritage, Beijing 100124, China*
[4]*Beijing Engineering Research Center of Historic Buildings Protection, Beijing 100124, China*
[5]*Shanghai Research Institute of Building Sciences, Shanghai 200032, China*

Correspondence should be addressed to Wei Qian; qianwei@bjut.edu.cn and Wei Wang; ieeww@bjut.edu.cn

Received 11 April 2019; Revised 27 June 2019; Accepted 4 July 2019; Published 14 August 2019

Academic Editor: Jorge Branco

It is currently known that using stress wave and drilling resistance to detect the internal damage in the ancient timber structure is not a highly precise process. To improve the detection precision of this process, a simulation test was used to detect the internal damage of poplar and elm in ancient buildings. In this empirical study, we compared the detection precision of these two detection methods. Based on the idea of variable weight, we introduced three combined forecasting models based on the IOWA operator, IOWGA operator, and IOWHA operator to predict the internal damage in the ancient timber structure. The results show that the combined forecasting model based on the IOWA operator is more effective in predicting compared to a single detection method and other combined forecasting models. To be more specific, the results show that the detection precision of the combined model is increased by 25.8% and 4.7%, respectively, compared to the precision of the stress wave and drilling resistance tests. The error indicators of the combined forecasting model based on the IOWA operator are better than those of the other combined forecasting models. In addition, the analysis results based upon cross-validation theory show the combined forecasting model based on the IOWA operator has the best applicability, which provides a new practical method for evaluating internal damage of timber components in ancient buildings.

1. Introduction

Ancient timber structures have high historical value, artistic value, and cultural value. Because wood is a natural material, it is easily affected by environmental factors during its life cycle. Split, insect attacks, hollow, decay, and other damages (see Figure 1) are easily found in the wooden components of ancient buildings. These may often result in some structural abnormalities of timber components [1]. Therefore, appropriately and precisely predicting the internal damage of timber components in ancient buildings is of great importance for sustaining the health and safety of ancient timber structures.

In recent years, national and international scholars have conducted many studies in detecting the internal damage of timber components in ancient buildings and have achieved good results. Commonly used nondestructive testing methods [2] for detecting the internal damage of timber components mainly include stress wave [3–5], X-ray scanning [6–8], drilling resistance [9–11], and ultrasonic wave [12–14]. However, it is difficult to achieve precise detection by using only one single detection method because each of these methods has its own advantages and disadvantages [15].

The basic principle of stress wave nondestructive testing is that one end of the wood is subjected to the impact force,

(a) (b) (c) (d)

Figure 1: Damaged characteristics of timber components: (a) hollow; (b) insect attacks; (c) crack; (d) decay.

and the stress wave propagates inside. The properties of the wood material are determined by measuring the change of the stress wave propagation velocity. Riggio et al. [8] stated stress waves could be used on-site for the identification of internal macroscopic defects in wooden structures. However, the described technique permits only qualitative and large-scale analysis. Other previous researches, however, have also shown the stress wave detection method is simple, convenient, fast, accurate, and of low cost, and it is not easily affected by the detection environment and suitable for field detection [16, 17]. In contrast, other studies found that the stress wave detection method should be improved. For instance, Li et al. [18] presented the stress wave velocity model to diagnosis the internal defects in urban trees. According to Guntekin et al. [19], the imaging results and detection precision still need to be improved, although many stress wave detection devices are capable of generating two-dimensional or three-dimensional tomographic images of wood cross sections. Sun and Wang [20] found that the two-dimensional image detected by the stress wave was not accurate enough to show the shape of the decayed area.

For X-ray scanning, since wood parts and wood defects have different X-ray absorption capacities, the image formed by the X-ray scanning technique is also different, and the internal defects of the wood can be measured according to a certain process identification analysis. Lechner et al. [6] found that X-rays allowed a view into the structural member or the connections. Riggio et al. [2] used X-rays to test the original roof timbers of the Saint Anne's Church in Prague, Czech Republic. The results showed when the loss of wood could not be determined visually, it is possible to estimate the extent of the void by measuring the dark area on the radiograph. Wei et al. [21], however, pointed out that X-rays had a low spatial resolution of the images when detecting wood defects. In addition, because of the high costs, equipment mobility issues, and health risks, this method is usually employed only in industrial environments [22]. For instance, Yu et al. [23] reported that the use of X-rays was neither portable nor practical in field assessment, and this approach posed a radiation hazard toward the users.

The drilling resistance method can quickly obtain the defect results inside the wood according to the resistance curve. Nowak et al. [11] used the drilling resistance method in in situ assessment of structural timber to assess the extent of wood damage in the tested elements. Nowak et al. also found that the drilling resistance graph was influenced by many factors, including angle and direction of drilling, interwood moisture, and drill bit sharpness. Chang et al. [24] and An et al. [25] found that the result detected by drilling resistance could only reflect the wood damage condition on the probe path; thus, it was difficult to give a specific and intuitive three-dimensional image. In order to obtain more precise information, more drilling resistance paths should be provided [26].

The ultrasonic spectrum technology primarily detects wood defects based on changes in the velocity of the ultrasonic waves in the wood. The last commonly used method to be examined is the ultrasonic wave method. Dackermann et al. [5] adopted the ultrasonic echo technique to obtain the direct localization of a reflector such as a backwall or any inhomogeneity or damage in the wood element. But it is difficult to locate the exact position of damage within the specimen and distinguish between one large irregularity such as a knot and a cluster of small ones. Perlin et al. [22] also used ultrasound to determine an accurate pith location. When applied to a given wood structure, this method can improve its structural assessment given by other nondestructive methods such as drilling resistance, stress wave transmission, and stress wave tomography. Due to the complexity of the wood structure, there are still problems to be solved by applying the ultrasonic technology. For example, the air gap between the ultrasonic probe and wood requires a good coupling agent [16].

Although many methods provide nondestructive assessment of the internal damage of old wood in timber structures, no single method can provide a complete data set for analysis [11]. In recent years, many scholars have used a combination of detection methods to detect internal damage of wood components [8, 15, 20, 24–31]. However, currently, there are not many methods to quantify uniformly the detection results detected by different methods. In order to overcome the loss of information caused by a single detection method and quantify uniformly the detection results, combined forecasting methods [32] are introduced to detect and predict the internal defects of wooden components. Chang et al. [24] proposed a combined forecasting method based on the Shapley value to predict the internal defects of wooden components. The weight coefficients of the stress wave and drilling resistance tests were fixed under each working condition, without considering the dynamics of the detected effects. However, the detected precision of this detection method is not the same under different working conditions. The detected precision is high under a certain working condition, but when it is under another different

working condition, it may be low. Therefore, this combined forecasting method could not provide a consistent precise prediction and still needs to be improved.

In order to overcome the disadvantage of assigning weight in the previous combined forecasting model, this paper introduced the idea of variable weight. According to the detected precision of a single detection method under various working conditions, the weight coefficients were given in an order from high to low. This greatly reduced the sensitivity of the result to a poor detection method. Additionally, it effectively improved the forecasting precision of the internal damage of wooden components in ancient buildings. The following four steps are used for evaluating the internal defect of wood components in ancient buildings based on the optimal combined forecasting model:

Step 1: considering the relative lower costs of equipment and simpler execution in field applications, test methods based on stress wave and drilling resistance were used to detect the internal defects of poplar and elm based on the idea of reverse simulation.

Step 2: based on the idea of variable weight and taking the square sum of error, square sum of logarithmic error, and square sum of reciprocal error as a guideline, three combined forecasting models were established based on the IOWA (induced ordered weighted average) operator [33–35], IOWGA (induced ordered weighted geometric average) operator [36, 37], and IOWHA (induced ordered weighted harmonic average) operator [38, 39]. Additionally, the combined forecasting models based on the entropy value [40, 41] and Shapley value [24–42] were used to compare with the proposed methods.

Step 3: based on the five indicators, a comprehensive evaluation index was developed to select the optimal combined forecasting model.

Step 4: according to the cross-validation theory [43], the optimal combined forecasting method was generalized into a model.

2. Nondestructive Tests

2.1. Specimen Fabrication. Poplar and elm, commonly used in ancient building timber components (e.g., beams and columns in the Guanyin Temple, Changzhi City, Shanxi Province), were selected as test specimens to simulate the hollow and insect attacks in the wooden structure. The raw materials were sawed into a cylindrical shape of 100 mm height (see Figure 2(a)), and the sawing plane of the test piece was required to be flat. Based on the cross-sectional area (S) of the test piece, there are five simulated damage ratios, which are, respectively, 1/32, 1/16, 1/8, 1/4, and 1/2 of the cross-sectional area (S) of the test piece (see Figure 2(b)). According to the method of reverse simulation, the internal hollow and insect attacks were simulated by manual digging (see Figure 2(c)) and drilling (see Figure 2(d)) in the cross sections of the wood component.

2.2. Test Hypothesis. Considering that wood is an anisotropic material, the physical properties of wood differ in different positions in the same tree. When the water content is the same, the wave propagation velocity increases linearly with the increase of density [44]. In the radial direction of the trunk, the change in wood density is divided into three cases: (1) increase from the bark to the pith, (2) first increase and then decrease from the bark to the pith, and (3) decrease from the bark to the pith [45]. To reduce the effect of this difference on the test results, we designed the damaged area of the test piece to be circular. Additionally, circular damaged areas of different sizes can better reflect the degree of internal damage of the wood. Therefore, we made two kinds of assumptions:

(1) It is assumed that the circumference of the specimen is a complete circle, regardless of the special shape of the wood

(2) It is assumed that the damage type of each specimen is a standard circle (see Figure 3)

2.3. Test Conditions. The indoor temperature is 20°C and the air relative humidity is 65%, which meet the requirements of the "Standard for test methods of timber structures" (GB/T 50329-2012). Test equipment includes Fakopp (stress wave test equipment) made in Hungary, IML-RESI PD500 (drilling resistance test equipment) and GANN-HT85T (wood hygrometer) made in Germany, and electric percussion drill (BOSCH), which are shown in Figure 4.

There are 18 working conditions in total. Each working condition simulates the detection of different defective areas of different tree species under different damage types. For example, the working condition 7 in Table 1 simulates a condition that the internal damage type of elm is hollow and the proportion of the damaged area is 1/4. Through visual inspection, surface percussion, and pressing, there are no obvious joints, splits, and other defects. Four specimens with an average moisture content of 9.18% are prepared for this test. They meet the requirements of the "Standard for design of timber structures" (GB 50005-2017) [46] and "Standard for test methods of timber structures" (GB/T 50329-2012) [47]. The specific parameters of the specimen are shown in Table 1.

2.4. Stress Wave Detection. Fakopp 3D Acoustic Tomograph is able to nondestructively detect the size and location of the defective part in wood. It works based on sound velocity measurement between several sensors around the trunk. If there is a hole, the sound waves will have to pass around the hole. Thus, they require more time to reach the opposite sensors. In order to explain the complex velocity model, a two-dimensional image is constructed. Healthy wood is shown in green, decaying wood is shown in red, and hollow is shown in blue. This test selected 10 sensors to detect the internal damage of the specimen (see Figure 5). The specific test steps were as follows:

(a) (b) (c) (d)

Figure 2: Fabrication of test specimens: (a) sawing; (b) damage ratio; (c) manual digging; (d) manual drilling.

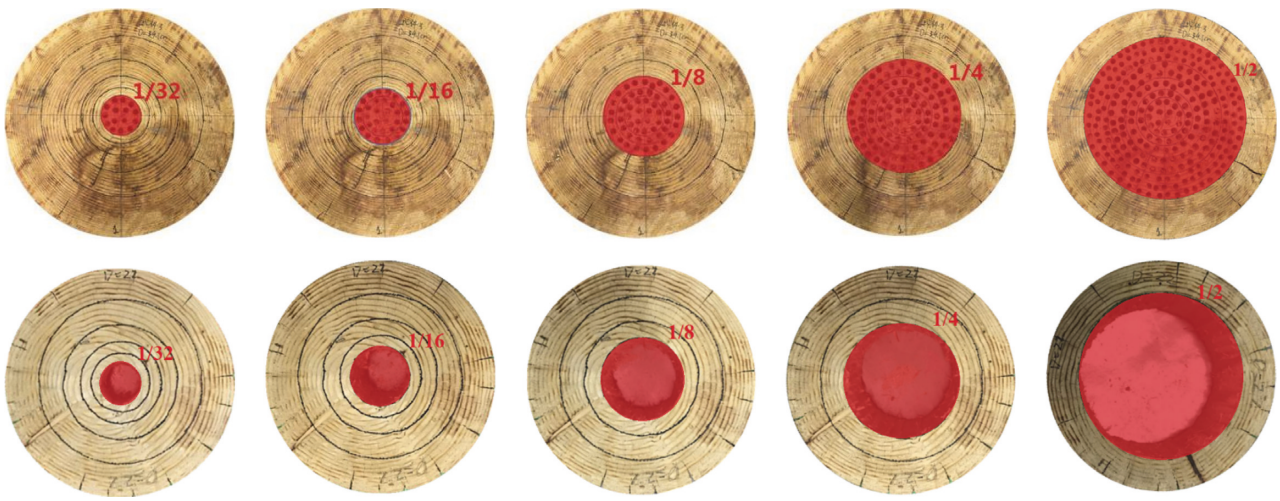

Figure 3: Shape of the simulated defective area.

(a) (b) (c) (d)

Figure 4: Specimen and test equipment. (a) Fakopp. (b) IML-RESI PD500. (c) GANN-HT85T. (d) BOSCH.

(1) 10 Sensors were placed around the specimen, connecting to the wood with steel nails
(2) Sensors were connected to amplifier boxes
(3) Bluetooth connection is established to PC
(4) Each sensor is tapped 3 times by a hammer
(5) The data are transmitted to a laptop to calculate the two-dimensional image

2.5. Drilling Resistance Tests. Drilling resistance tests are based on microdrilling of wood at a constant velocity by a standard drill. IML-RESI PD500 has a small needle driven by a motor to penetrate into the wood at a constant speed. When the drilling needle enters the interior of the wood, it encounters relative resistance in both directions which are the forward direction and the direction of rotation. The relative resistance value varies with the density of each tree species, and the instrument records the relative resistance during the test. The resistance image processing software (PD-Tools Pro) is applied to export the data information to Excel, which can be used to draw two-dimensional images of relative resistance. In the figure, the abscissa represents the path length and the ordinate represents the relative resistance that the drilling needle encounters. Based on the measured impedance curve, the width of the damaged area can be determined according to the changes in the peaks and troughs in the curve (see Figures 6(b) and 6(d)). The decay inside the wood can be judged [48, 49], and the test steps are as follows:

Table 1: Parameters of test specimens.

Working condition	Damaged proportion	Simulation type	Tree species	Radius (mm)	Height (mm)	Moisture content (%)	Detected height (mm)
1	1/16	Hollow	Poplar (specimen 1)	115.4	100	9.4	50
2	1/8						
3	1/4						
4	1/32	Hollow	Elm (specimen 2)	111.5	100	8.7	50
5	1/16						
6	1/8						
7	1/4						
8	1/2						
9	1/32	Insect attacks	Poplar (specimen 3)	172.3	100	9.7	50
10	1/16						
11	1/8						
12	1/4						
13	1/2						
14	1/32	Insect attacks	Elm (specimen 4)	114.6	100	8.9	50
15	1/16						
16	1/8						
17	1/4						
18	1/2						

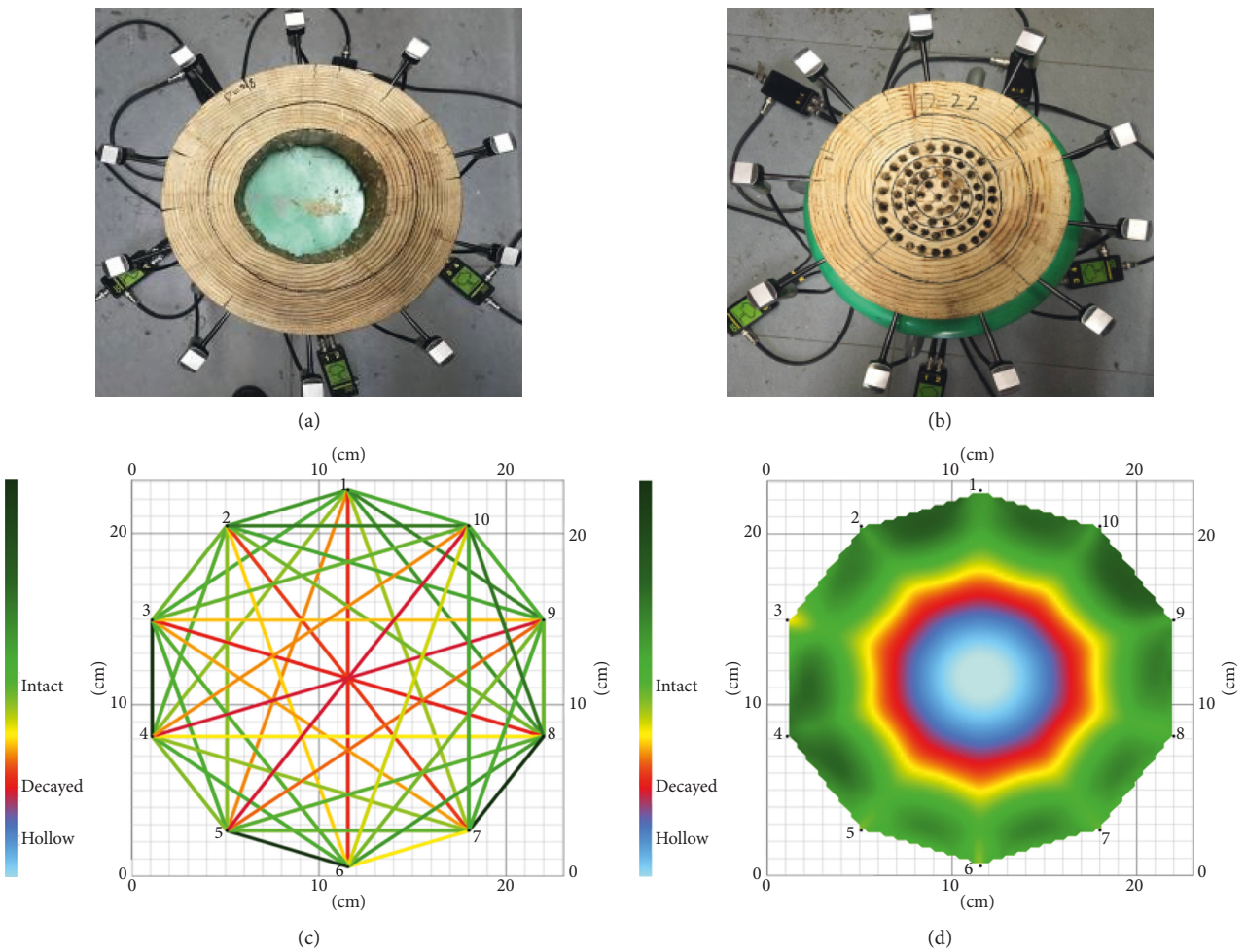

Figure 5: Stress wave tests: (a) hollow; (b) insect attacks; (c) wave velocity diagram; (d) two-dimensional image.

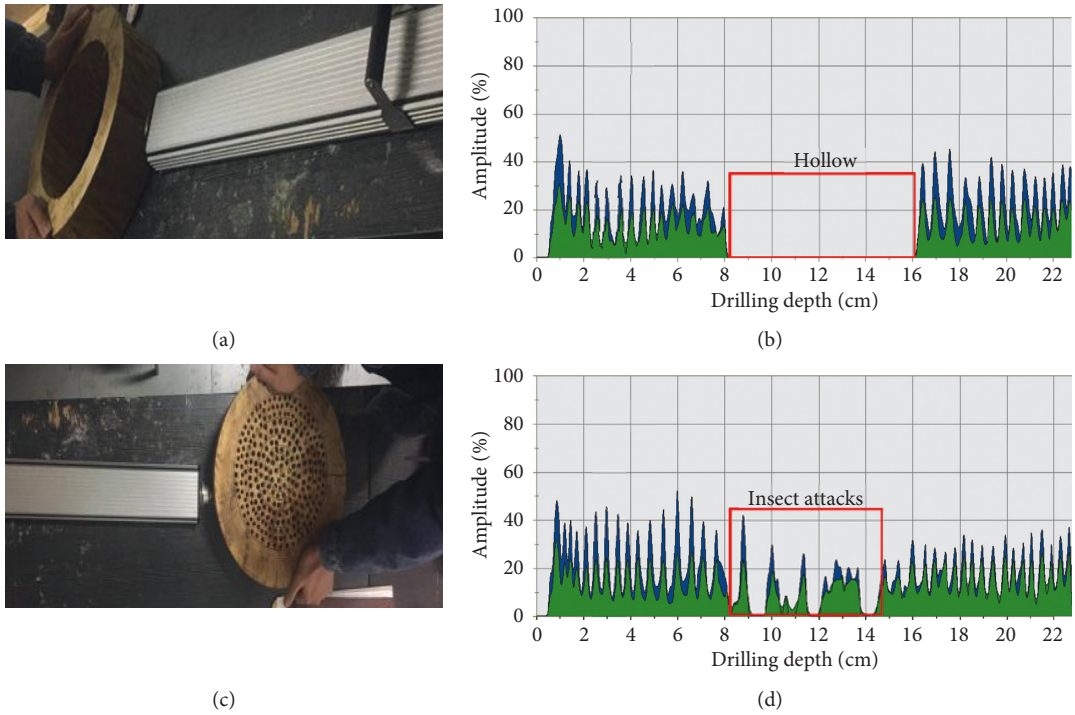

Figure 6: Drilling resistance tests: (a) hollow and (b) its two-dimensional image; (c) insect attacks and (d) their two-dimensional image.

(1) Three paths are selected for the test specimen.

(2) The bit should be perpendicular to the direction of the rings (see Figures 6(a) and 6(c)).

(3) The drilling needle rotation rate and advance rate parameters of the test equipment are set, respectively. The stability of the drilling resistance test equipment should be ensured.

3. Discussion and Analysis of Test Results

3.1. Two-Dimensional Images. For example, in specimen 2, the tree species is elm and the simulated defect type is hollow. Because of limited pages, Figure 7 only shows the relative impedance curve in one path direction.

When there is no internal damage in the specimen (see Figure 7(a)), the two-dimensional image detected by stress wave tests is green, and the relative impedance curve detected by drilling resistance tests is continuous. Two detection methods indicate that the specimen is healthy wood. While the internal hollow is small (when the damaged proportion is less than 1/8), pale yellow (see Figure 7(b)) and red (see Figure 7(c)) colors are presented in the center of the two-dimensional image detected by stress wave tests. However, the relative impedance curve image detected by the drilling resistance tests starts to appear "blank" reflecting the approximate width of the hollow area. With the expansion of the internal hollow area, the center part of the two-dimensional image detected by stress wave tests shows a bright blue color. The stress wave tests are more accurate in identifying the size and location of internal hollow (see Figures 7(d)–7(f)). The stress wave tests visually express the location and size of internal hollow through colors, but the boundary of the hollow is relatively fuzzy. For drilling resistance tests, the length of the "blank" on the relative impedance curve increases with the expansion of the internal hollow area, which is basically similar to the test results detected by stress wave tests.

To sum up, the stress wave tests can quickly make an intuitive judgment on the general position and degree of damage, but the judgment on the damage type is weak and the boundary division of internal defects is fuzzy. However, the drilling resistance tests only reflect the internal damage of the wooden components under one path according to the relative impedance curve. It is not possible to detect every position of a cross section, and there is no great reference value when used alone. If enough information is needed, more drilling resistance paths should be provided. Through analysis, it is found that the stress wave image and the resistance curve have a good correspondence relationship in this test. Putting the results of the two together for comparative analysis can make up for their respective shortcomings.

3.2. Detection Data. The detection data listed in Table 2 show that the detected precision of the same detection method is different while it is working in various working conditions. The mean error and mean precision obtained by stress wave tests are 11.13 cm^2 and 72.9%, respectively, while the mean error and mean precision obtained by drilling resistance tests are 8.47 cm^2 and 87.6%, respectively. The correlation coefficients between the detected data obtained by stress wave and drilling resistance tests and the actual value are 0.9894 and 0.9989. The overall detection effect of drilling

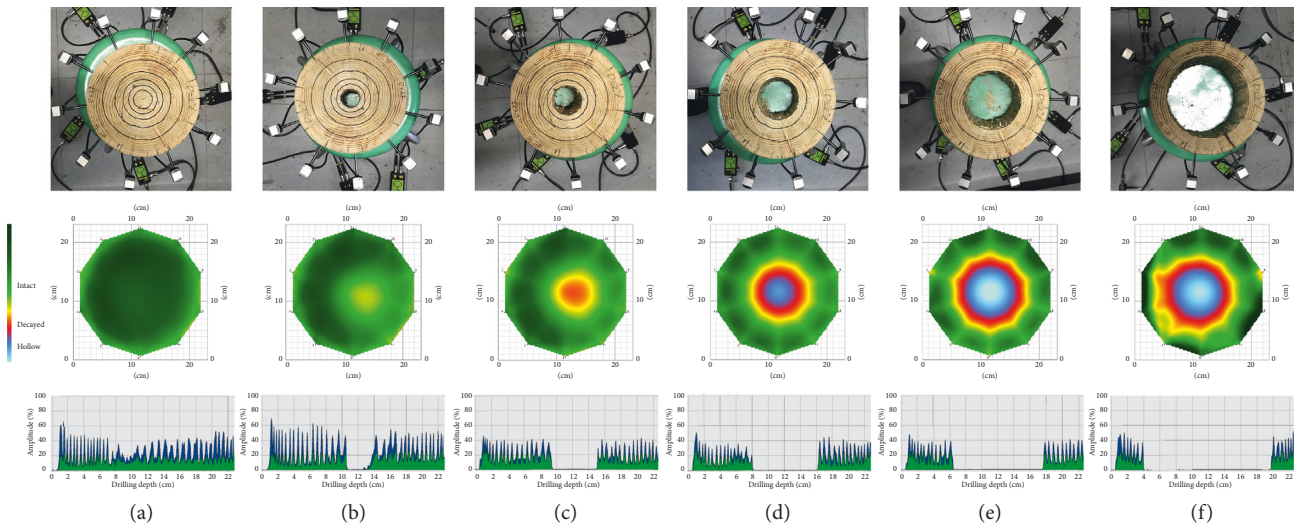

Figure 7: Detection of two-dimensional images of specimen 2: (a) 0; (b) 1/32; (c) 1/16; (d) 1/8; (e) 1/4; (f) 1/2.

Table 2: Results of two detection methods.

Working condition	Damaged proportion	Simulation type	Tree species	True value (cm^2)	Stress wave			Drilling resistance		
					Detection value (cm^2)	Absolute error (cm^2)	Detected precision (%)	Detection value (cm^2)	Absolute error (cm^2)	Detected precision (%)
1	1/16	Hollow	Poplar (specimen 1)	26.13	37.22	11.09	57.6	21.34	4.79	81.7
2	1/8			52.27	70.59	18.32	65.0	44.12	8.15	84.4
3	1/4			104.54	124.64	20.10	80.8	95.02	9.52	90.9
4	1/32	Hollow	Elm (specimen 2)	12.20	3.90	8.30	32.0	7.47	4.73	61.2
5	1/16			24.40	15.61	8.79	64.0	18.02	6.38	73.9
6	1/8			48.80	58.55	9.75	80.0	39.49	9.31	80.9
7	1/4			97.59	109.3	11.71	88.0	88.08	9.51	90.3
8	1/2			195.18	202.98	7.80	96.0	184.03	11.15	94.3
9	1/32	Insect attacks	Poplar (specimen 3)	29.13	15.93	13.20	54.7	28.17	0.96	96.7
10	1/16			58.26	44.65	13.61	76.6	55.97	2.29	96.1
11	1/8			116.52	101.53	14.99	87.1	104.2	12.32	89.4
12	1/4			233.04	225.68	7.36	96.8	219.89	13.15	94.4
13	1/2			466.09	471.57	5.48	98.8	449.68	16.41	96.5
14	1/32	Insect attacks	Elm (specimen 4)	12.89	4.13	8.76	32.0	11.93	0.96	92.6
15	1/16			25.77	10.94	14.83	42.5	22.68	3.09	88.0
16	1/8			51.55	34.06	17.49	66.1	46.83	4.72	90.8
17	1/4			103.10	107.24	4.14	96.0	87.57	15.53	84.9
18	1/2			206.19	210.81	4.62	97.8	186.77	19.42	90.6
Average value						11.13	72.9		8.47	87.6

resistance tests is more precise compared to that of stress wave tests.

Although the correlation coefficients between the two sets of test data and the real value are very high, the detected precision is still low under some conditions, especially when the stress wave detection is used. We find that the detected precision of the stress wave tests under working condition 1, working condition 4, working condition 9, working condition 14, and working condition 15 is relatively low. The proportion of damage simulated under the five working conditions is also small. Therefore, it is of great engineering value to study the precision of stress wave detection with such a small internal damaged proportion.

When we examined the curves of detected precision under different working conditions (see Figure 8), we found that the detected precision obtained by stress wave tests increases with the increase of the internal damaged area in the wood.

As far as drilling resistance tests are concerned, the detected precision increases with the increase of the internal defects in the wood when the internal damage type is hollow (see Figures 8(a) and 8(b)). While the internal damage type is insect attacks, the detected precision of specimen 3 does not change much with the increase of insect attack area (see Figures 8(c) and 8(d)).

In addition, when the internal defects are small, the detected precision of drilling resistance tests is higher than that of stress wave tests. With the further increase of

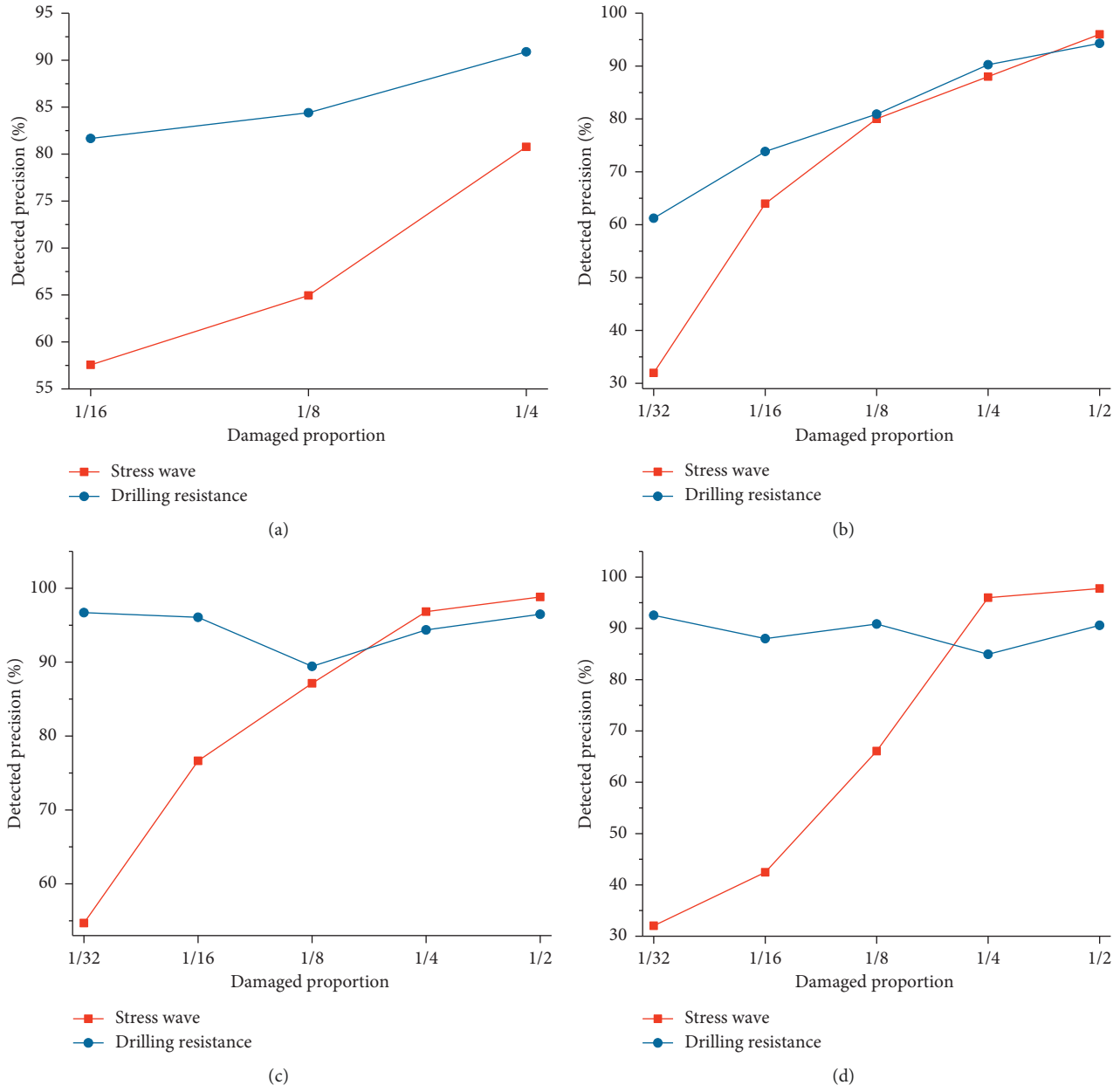

Figure 8: Curves of detected precision under different working conditions. (a) Specimen 1. (b) Specimen 2. (c) Specimen 3. (d) Specimen 4.

simulated damaged area, the detected precision of both detection methods tends to be close to each other. When the internal damaged proportion of wood exceeds 1/4, the detected precision of stress wave tests is higher than that of drilling resistance tests (see Figures 8(b)–8(d)).

To sum up, comprehensive use of stress wave and drilling resistance tests can screen the type, position, and size of internal damage of timber components. However, the detection results of the two detection methods are quite different with low detected precision. In order to comprehensively use the information provided by the two detection methods, this paper introduces several new combined forecasting models which are different from the literature [24], in order to improve the prediction precision of the internal damage in ancient building wood components.

4. Combined Forecasting Model

4.1. Model Building. Based on the OWA operator [50], OWGA operator [51], and OWHA operator [38], great deals of extensions have been developed. These extensions are the IOWA operator, IOWGA operator, and IOWHA operator. In this study, we reordered the arguments by an inducing variable.

If there are m feasible single detection methods to detect internal defects of the timber components in ancient buildings under a certain working condition, the detection value of the i-th detection method in the t-th working condition is x_{it}, where $i = 1, 2, \ldots, m$ and $t = 1, 2, \ldots, N$.

If l_m is the weight of the m-th single detection in the combined forecasting model, the weight satisfy the normalization and nonnegativity, such that

$$\sum_{i=1}^{m} l_i = 1, \quad l_i \geq 0,\ i = 1, 2, \ldots, m,$$

$$a_{it} = \begin{cases} 1 - \left|\dfrac{(x_t - x_{it})}{x_t}\right|, & \text{if} \left|\dfrac{(x_t - x_{it})}{x_t}\right| < 1, \\ 0, & \text{if} \left|\dfrac{(x_t - x_{it})}{x_t}\right| \geq 1, \end{cases}$$

$$i = 1, 2, \ldots, m,\ t = 1, 2, \ldots, N, \tag{1}$$

where a_{it} represents the detected precision of the i-th detection method under the t-th working condition, $a_{it} \in [0, 1]$. When a_{it} is regarded as the inducement value of x_{it}, it can form m two-dimensional arrays which are (a_{1t}, x_{1t}), (a_{2t}, x_{2t}), …, (a_{mt}, x_{mt}). The detected precision sequence $(a_{1t}, a_{2t}, \ldots, a_{mt})$ of m detection methods under the t-th working condition is arranged from high to low. Let us hypothesize that a-index(it) is a subscript of the i-th largest value among the detection sequence.

(1) Model based on the IOWA operator [34]: the square sum of error is taken as the criterion to establish the combined forecasting model. According to the detected precision sequence, the combined forecasting value based on the IOWA operator can be obtained by

$$I_L[(a_{1t}, x_{1t}), (a_{2t}, x_{2t}), \ldots, (a_{mt}, x_{mt})] = \sum_{i=1}^{m} l_i x_{a-\text{index}(it)}. \tag{2}$$

The optimal combined forecasting model based on the IOWA operator with the square sum of error as the criterion can be expressed as follows:

$$S_{\text{IOWA}} = \sum_{t=1}^{N} \left(x_t - \sum_{i=1}^{m} l_i x_{a-\text{index}(it)} \right)^2. \tag{3}$$

(2) Model based on the IOWGA operator [36]: the square sum of logarithmic error is taken as the criterion to establish the combined forecasting model. According to the detected precision sequence, the combined forecasting value based on the IOWGA operator can be obtained by

$$G_L[(a_{1t}, x_{1t}), (a_{2t}, x_{2t}), \ldots, (a_{mt}, x_{mt})] = \prod_{i=1}^{m} x_{a-\text{index}(it)}^{l_i}. \tag{4}$$

The optimal combined forecasting model based on the IOWGA operator with the square sum of logarithmic error as the criterion can be expressed as follows:

$$S_{\text{IOWGA}} = \sum_{t=1}^{N} \left(\ln x_t - \ln \prod_{i=1}^{m} x_{a-\text{index}(it)}^{l_i} \right)^2. \tag{5}$$

(3) Model based on the IOWHA operator [38]: the square sum of reciprocal error is taken as the criterion to establish the combined forecasting model. According to the detected precision sequence, the combined forecasting value based on the IOWHA operator can be obtained by

$$H_L[(a_{1t}, x_{1t}), (a_{2t}, x_{2t}), \ldots, (a_{mt}, x_{mt})] = \frac{1}{\sum_{i=1}^{m} \left(l_i / x_{a-\text{index}(it)} \right)}. \tag{6}$$

The optimal combined forecasting model based on the IOWHA operator with the square sum of reciprocal error as the criterion can be expressed as follows:

$$S_{\text{IOWHA}} = \sum_{t=1}^{N} \left(\sum_{i=1}^{m} l_i \left(\frac{1}{x_t} - \frac{1}{x_{a-\text{index}(it)}} \right) \right)^2. \tag{7}$$

4.2. Solving Model. Taking the simulated hollow test of specimen 1 as an example, we can list the two-dimensional array of detection values and its detected precision under the t-th working condition as follows:

$$\begin{bmatrix} (0.576, 37.22), & (0.817, 21.34) \\ (0.650, 70.59), & (0.844, 44.12) \\ (0.808, 124.64), & (0.909, 95.02) \end{bmatrix}. \tag{8}$$

The prediction value based on the IOWA operator is calculated according to equation (2). The solving process is shown as follows:

$$\begin{aligned} I_L[(a_{11}, x_{11}), (a_{21}, x_{21})] &= 21.34 l_1 + 37.22 l_2, \\ I_L[(a_{12}, x_{12}), (a_{22}, x_{22})] &= 44.12 l_1 + 70.59 l_2, \\ I_L[(a_{13}, x_{13}), (a_{23}, x_{23})] &= 95.02 l_1 + 124.64 l_2. \end{aligned} \tag{9}$$

By substituting them into equation (3), the optimal combined forecasting model based on the IOWA operator is arranged as follows:

$$\begin{aligned} \min \quad & S_{\text{IOWA}}(l_1, l_2) = (26.13 - 21.34 l_1 - 37.22 l_2)^2 + (52.27 - 44.12 l_1 - 70.59 l_2)^2 + (104.54 - 95.02 l_1 - 124.64 l_2)^2, \\ \text{s.t.} \quad & \begin{cases} l_1 + l_2 = 1, \\ l_1 \geq 0,\ l_2 \geq 0. \end{cases} \end{aligned} \tag{10}$$

The MATLAB software is used to solve the optimal weight (l_i). Some parameters of the genetic algorithm are set as follows:

Generations = 50

StallGenLimi = 100

PopInitRange = [zeros(1, m); ones(1, m)]

PopulationSize = 10000

After 50 genetic iterations, the MATLAB software shows that (l_1, l_2) is (0.69, 0.31), respectively. The black and blue points in Figure 9 are the best fitness value and the mean fitness value, respectively. It is found that the mean fitness value of the population represents a smooth downward trend with the increase of the number of iterations and gradually moves towards the best fitness value (see Figure 9).

Similarly, the solving processes of the models based on the IOWGA operator and IOWHA operator are the same as that of the model based on the IOWA operator. In order to select the optimal model, the traditional combined forecasting models based on the entropy value and Shapley value are introduced in this paper for comparison.

4.3. Analyzing Precision of Different Combined Forecasting Models. In Table 3, the mean precision from large to small is P_1, P_2, P_3, P_4, and P_5. Compared to detected precision of stress wave tests, the precision is improved by 25.8%, 25.4%, 25.2%, 21.5%, and 17.6%, respectively. While compared to detected precision of drilling resistance tests, the precision is improved by 4.7%, 4.3%, 4.2%, 1.1%, and 2.2%, respectively. Additionally, the mean absolute error from small to large is e_1, e_2, e_3, e_5, and e_4. So, we find that the models based on the IOWA operator, IOWGA operator, and IOWHA operator have better forecasting effects compared to others (see Figure 10).

Other than that, through statistical analysis of working condition 1, working condition 4, working condition 9, working condition 14, and working condition 15 (see Table 4), we also find that the combined forecasting models based on the IOWA operator, IOWGA operator, and IOWHA operator are more effective compared to the combined forecasting models based on the entropy value and Shapley value in improving the detected precision of stress wave tests in the case of small defects inside the wood.

4.4. Forecasting Effect Evaluation. According to the evaluation principle of the forecasting effect, SSE, MSE, MAE, MAPE, and MSPE are selected as evaluation indexes to reflect the effectiveness of the combined forecasting models. The calculation results are shown in Table 5:

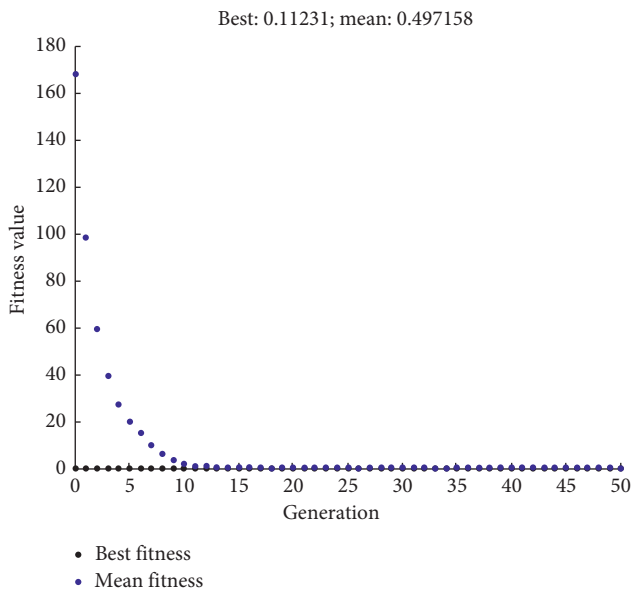

Figure 9: Best fitness value and mean fitness value.

$$\mathrm{SSE} = \sum_{t=1}^{n} (x_t - \hat{x}_t)^2,$$

$$\mathrm{MSE} = \frac{1}{n}\sqrt{\sum_{t=1}^{n} (x_t - \hat{x}_t)^2},$$

$$\mathrm{MAE} = \frac{1}{n}\sum_{t=1}^{n} \left|x_t - \hat{x}_t\right|, \tag{11}$$

$$\mathrm{MAPE} = \frac{1}{n}\sum_{t=1}^{n} \left|\frac{(x_t - \hat{x}_t)}{x_t}\right|,$$

$$\mathrm{MSPE} = \frac{1}{n}\sqrt{\sum_{t=1}^{n} \left[\frac{(x_t - \hat{x}_t)}{x_t}\right]^2}.$$

In Table 5, it is found that the first four indexes of the combined forecasting method based on the IOWA operator are significantly lower than those of others. Although MSPE of the combined forecasting method based on the IOWA operator is not the least, it is close to MSPE of combined forecasting methods based on the IOWGA operator and IOWHA operator. Therefore, the combined forecasting model based on the IOWA operator has the best effect. Meanwhile, by normalizing the above five indexes, the expression of the comprehensive evaluation index C is obtained as follows:

$$C_i = \frac{1}{n}\sum_{j=1}^{n} \frac{\min\left(E_j\right)}{E_{ij}}, \tag{12}$$

Table 3: Results of each combined forecasting model.

Working condition	IOWA			IOWGA			IOWHA			Entropy			Shapley		
	S_1	e_1	P_1 (%)	S_2	e_2	P_2 (%)	S_3	e_3	P_3 (%)	S_4	e_4	P_4 (%)	S_5	e_5	P_5 (%)
1	26.32	0.19	99.3	26.09	0.04	99.9	26.09	0.04	99.9	28.41	2.28	91.3	23.31	2.82	89.2
2	52.42	0.15	99.7	52.29	0.02	99.9	52.53	0.26	99.5	55.90	3.63	93.1	47.41	4.86	90.7
3	104.31	0.23	99.8	104.81	0.27	99.7	105.75	1.21	98.8	108.20	3.66	96.5	98.70	5.84	94.4
4	5.99	6.21	49.1	7.47	4.73	61.2	7.47	4.73	61.2	6.17	6.03	50.6	5.90	6.30	48.4
5	17.02	7.38	69.8	18.02	6.38	73.9	18.02	6.38	73.9	17.14	7.26	70.3	16.96	7.44	69.5
6	47.41	1.39	97.2	39.49	9.31	80.9	39.49	9.31	80.9	46.42	2.38	95.1	47.87	0.93	98.1
7	96.90	0.70	99.3	88.08	9.51	90.3	88.08	9.51	90.3	95.79	1.80	98.2	97.41	0.18	99.8
8	195.11	0.07	99.9	202.98	7.80	96.0	202.98	7.80	96.0	190.92	4.26	97.8	192.36	2.82	98.6
9	28.07	1.06	96.4	28.17	0.96	96.7	28.17	0.96	96.7	25.75	3.38	88.4	23.22	5.91	79.7
10	55.87	2.39	95.9	55.97	2.29	96.1	55.97	2.29	96.1	53.73	4.53	92.2	51.39	6.87	88.2
11	104.18	12.34	89.4	104.20	12.32	89.4	104.20	12.32	89.4	103.67	12.85	89.0	103.12	13.40	88.5
12	225.63	7.41	96.8	225.68	7.36	96.8	225.68	7.36	96.8	221.03	12.01	94.8	222.23	10.81	95.4
13	471.38	5.29	98.9	471.57	5.48	98.8	471.57	5.48	98.8	454.00	12.09	97.4	458.54	7.55	98.4
14	11.41	1.48	88.5	11.93	0.96	92.6	11.93	0.96	92.6	11.38	1.51	88.3	8.54	4.35	66.3
15	21.90	3.87	85.0	22.68	3.09	88.0	22.68	3.09	88.0	21.86	3.91	84.8	17.58	8.19	68.2
16	45.98	5.57	89.2	46.83	4.72	90.8	46.83	4.72	90.8	45.94	5.61	89.1	41.28	10.27	80.1
17	105.93	2.83	97.3	107.24	4.14	96.0	107.24	4.14	96.0	88.95	14.15	86.3	96.12	6.98	93.2
18	209.21	3.02	98.5	210.81	4.62	97.8	210.81	4.62	97.8	188.45	17.74	91.4	197.22	8.97	95.6
Mean value		3.42	91.7		4.67	91.4		4.73	91.3		6.61	88.6		6.36	85.7

Note. S_i: forecasting value of different combined forecasting models, $i = 1, 2, 3, 4, 5$ (unit: cm^2); e_i: absolute error of different combined forecasting models, $i = 1, 2, 3, 4, 5$ (unit: cm^2); P_i: precision of different combined forecasting models, $i = 1, 2, 3, 4, 5$.

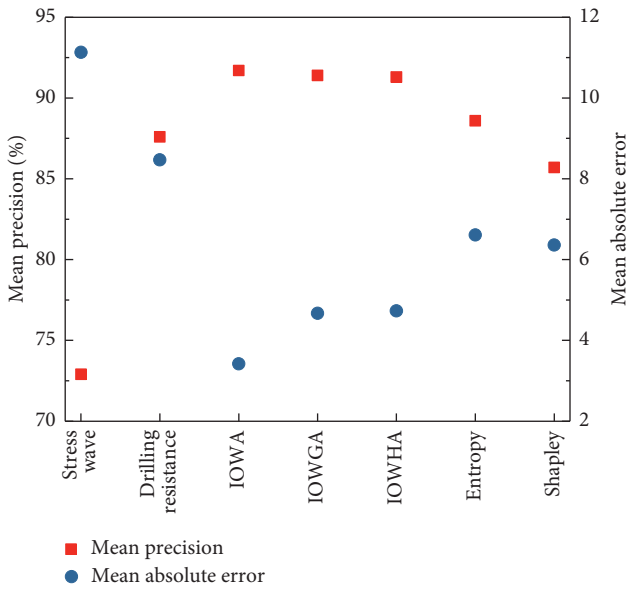

Figure 10: Curves of mean precision and mean absolute error.

where C_i is the comprehensive evaluation index of the i-th method, $i = 1, 2, \ldots, M$; E_{ij} is the j-th index of the i-th method, $j = 1, 2, \ldots, n$; and $\min(E_j)$ is the minimum value among the j-th indexes of m methods. The higher the C is, the better the corresponding combined forecasting model is. The index C of each method is developed by bringing the five index values in Table 5 into equation (12).

Figure 11 shows that the comprehensive evaluation index of each combined forecasting model is significantly higher than that of the two single detection methods, indicating that the combined forecasting model can improve the forecasting precision of the internal defects of the timber components. Furthermore, the C of the combined forecasting model based on the IOWA operator is 97.2%, higher than others. All the analysis shows that the combined forecasting model based on the IOWA operator is the optimal model, followed by the combined forecasting models based on the IOWGA operator and IOWHA operator.

5. Applicability Assessment

An applicability assessment is performed for the combined forecasting models based on the IOWA operator, IOWGA operator, and IOWHA operator.

5.1. Cross-Validation Theory. Since there are a total of 18 working conditions in this test, each working condition has a corresponding set of actual values and detected values obtained by stress wave and drilling resistance tests (see Table 2). Because of the small number of data samples, and each combined forecasting model is tested only once, the randomness is large, which does not prove that the above optimal models have good universality. In order to make full use of the data samples, a cross-validation method is applied to carry out the test. The research process is shown in Figure 12.

Firstly, by setting random samples, we randomly extracted N ($N = 5, 6, \ldots, 17$) working conditions from 18 working conditions as a training set (I_N), and then the corresponding remaining $18 - N$ working conditions are considered as a testing set ($\overline{I}_N$). For the number (N) of randomly selected samples, there are C_{18}^N subsets for both the training set and the testing set (see Table 6). For example, if $N = 5$, both the training set (I_5) and the testing set ($\overline{I}_5$) will have 8568 subsets.

Table 4: Comparison of detected precision and forecasting precision of stress wave tests under several working conditions.

Working condition	Damaged proportion	Stress wave (%)	IOWA (%)	IOWGA (%)	IOWHA (%)	Entropy (%)	Shapley (%)
1	1/16	57.6	99.3	99.9	99.9	91.3	89.2
4	1/32	32.0	49.1	61.2	61.2	50.6	48.4
9	1/32	54.7	96.4	96.7	96.7	88.4	79.7
14	1/32	32.0	88.5	92.6	92.6	88.3	66.3
15	1/16	42.5	85.0	88.0	88.0	84.8	68.2

Table 5: Evaluation indexes of the forecasting effect.

Method		SSE	MSE	MAE	MAPE	MSPE
Stress wave		2611.2	2.839	11.13	0.271	0.082
Drilling resistance		1795.7	2.354	8.466	0.124	0.036
Combined forecasting model	IOWA	402.878*	1.115*	3.421*	0.083*	0.036
	IOWGA	614.489	1.377	4.667	0.086	0.031*
	IOWHA	615.947	1.379	4.732	0.087	0.031*
	Entropy	1199.338	1.924	6.616	0.114	0.038
	Shapley	925.767	1.690	6.361	0.143	0.047

Note. *Minimum value.

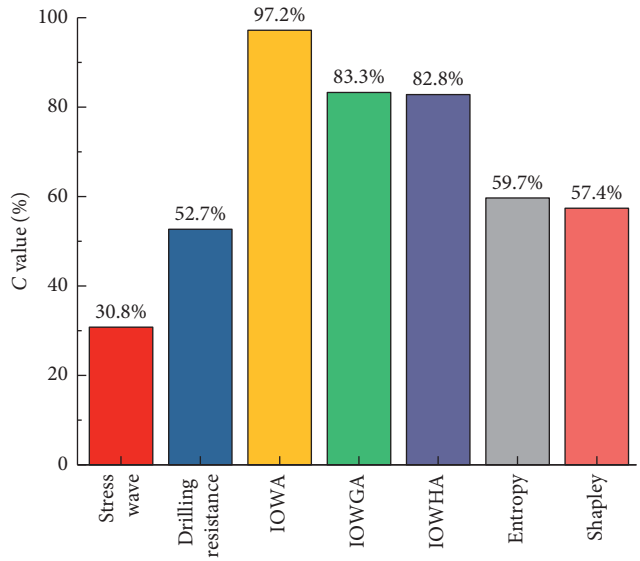

Figure 11: Histograms of the index C.

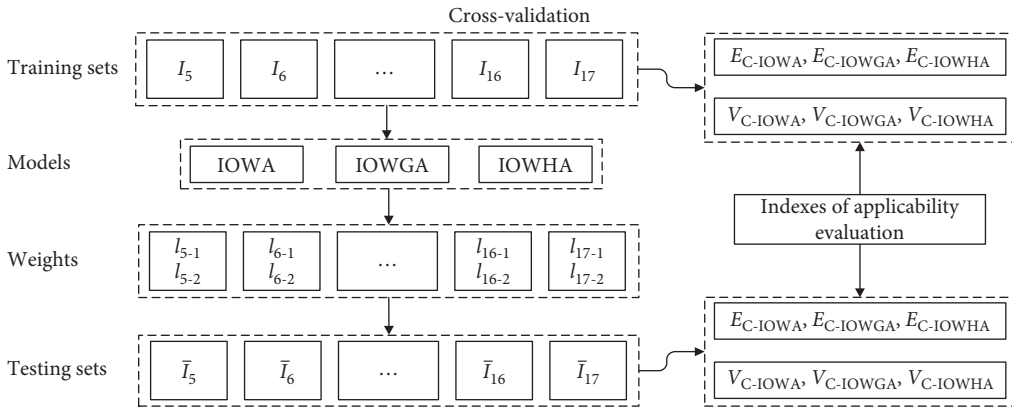

Figure 12: Flowchart for cross-validation.

Table 6: Number of samples in each subset.

Training set (testing set)	I_5 ($\overline{I}_5$)	I_6 ($\overline{I}_6$)	I_7 ($\overline{I}_7$)	I_8 ($\overline{I}_8$)	I_9 ($\overline{I}_9$)	I_{10} ($\overline{I}_{10}$)	I_{11} ($\overline{I}_{11}$)	I_{12} ($\overline{I}_{12}$)	I_{13} ($\overline{I}_{13}$)	I_{14} ($\overline{I}_{14}$)	I_{15} ($\overline{I}_{15}$)	I_{16} ($\overline{I}_{16}$)	I_{17} ($\overline{I}_{17}$)
Sample number	5 (13)	6 (12)	7 (11)	8 (10)	9 (9)	10 (8)	11 (7)	12 (6)	13 (5)	14 (4)	15 (3)	16 (2)	17 (1)
Combinatorial number	8568	18564	31824	43758	48620	43758	31824	18564	8568	3060	860	153	18

If I_5 = {working condition 1, working condition 2, working condition 3, working condition 4, working condition 5}, then $\overline{I}_5$ = {working condition 6, working condition 7, working condition 8, working condition 9, working condition 10, working condition 11, working condition 12, working condition 13, working condition 14, working condition 15, working condition 16, working condition 17}.

By analogy, we can get 8568 subsets for the training set (I_5) and the testing set ($\overline{I}_5$).

Secondly, based on random sample data in each training set (I_N), three combined forecasting models based on the IOWA operator, IOWGA operator, and IOWHA operator are established to solve three sets of corresponding optimal weights. Based on the cross-validation method, three sets of weights are substituted into the corresponding testing set ($\overline{I}_N$). For the training set and testing set, we can get the comprehensive evaluation index C corresponding to each combined forecasting model using equation (12).

Finally, we calculate the mean value (E_C) and variance (V_C) of the comprehensive evaluation index C. Through the statistical analysis of the change law of the mean value (E_C) and variance (V_C), the universality of the optimal combined forecasting model is judged.

5.2. Cross-Validation Result Analysis. The mean value (E_C) and the variance (V_C) of the comprehensive evaluation indexes are evaluated by each combined forecasting model in the training sets (see Table 7).

In Table 7, we find that $E_{\text{C-IOWA}}$ of each training set has a significantly higher value compared to $E_{\text{C-IOWGA}}$ and $E_{\text{C-IOWHA}}$. The higher the E_C is, the better the overall forecasting precision is. The alignment of the variance of the comprehensive evaluation indexes is $V_{\text{C-IOWA}} < V_{\text{C-IOWGA}} < V_{\text{C-IOWHA}}$. The smaller the V_C is, the smaller the dispersion of the C value is and the more stable the data change is. This indicates that the combined forecasting model based on the IOWA operator is well applicable.

In Figure 13, the distribution maps of E_C and V_C corresponding to each training set show a roughly linear changing trend. When the sample data in the training set (I_N) increase, $E_{\text{C-IOWA}}$ and $E_{\text{C-IOWH}}$ increase and $E_{\text{C-IOWGA}}$ decreases. With the increase of the number of sample data in the training sets, the V_C of the three combined forecasting models decreases. But the change of $V_{\text{C-IOWA}}$ is smallest, indicating that the C does not fluctuate much and the data are very stable.

Based on the cross-validation theory, the optimal weights obtained by each training set are brought into the corresponding testing set. E_C and V_C of the testing sets are listed in Table 8, and the distribution maps of E_C and V_C calculated by each testing set are shown in Figure 14.

In Table 8, $E_{\text{C-IOWA}}$ of testing sets is significantly higher than $E_{\text{C-IOWGA}}$ and $E_{\text{C-IOWHA}}$, while $V_{\text{C-IOWA}}$ is significantly lower than $V_{\text{C-IOWGA}}$ and $V_{\text{C-IOWHA}}$. However, it is noted the values of $E_{\text{C-IOWGA}}$ and $E_{\text{C-IOWHA}}$ or $V_{\text{C-IOWGA}}$ and $V_{\text{C-IOWHA}}$ are very close to each other. Meanwhile, it is found from Figure 14 that E_C corresponding to each testing set decreases with the decrease of the sample number in the testing sets. Contrarily, V_C increases with the decrease of the sample number in the testing sets. The distribution map of $V_{\text{C-IOWA}}$ has little change in slope, meaning the corresponding C value is more stable. The results show that the combined forecasting model based on the IOWA operator has the highest overall forecasting precision and best level of applicability among the three models.

6. Nondestructive Tests for Double-Cirold Longevity Pavilion

Double-Cirold Longevity Pavilion is located in the Beijing Tiantan Park. It was built in the Middle Qing Dynasty and has a history of 277 years. Double-Cirold Longevity Pavilion is a combination of two round pavilions with double eaves and spires. Its structure is peculiar and precise, and its shape is novel and well proportioned. This kind of pavilion has high scientific, artistic, and cultural value in the Chinese timber structure. Affected by the natural environment and human factors all year round, timber components are damaged. Eventually, it leads to the loss of the external protective layer for timber components and the acceleration of the internal and external damage of timber components.

Nondestructive tests of timber components of the double-ring marsupial pavilion were performed by stress wave and drilling resistance (see Figure 15). It was found that the beams and the columns had internal defects. The B2 column of Double-Cirold Longevity Pavilion is an example with a moisture content of 9.8%. The perimeter of the wooden column is 109.9 cm, and the detected section area is 961.63 cm^2. According to the two-dimensional image obtained by the stress wave tests, the internal defects were located. Drilling resistance tests were conducted pertinently. There were two detected paths in drilling resistance tests, and each path passed through the location of defects.

Through nondestructive tests, it was found that there was an uncompacted sound when knocking the position of the B2 column, 400 mm from the ground. A certain degree of defect is found in the interior wood by the stress wave tests (see Figure 16). The damaged area detected by the stress wave tests accounts for 18% of the detected section, and the damaged area is 173.09 cm^2. The drilling resistance tests show the damaged area is 49 cm^2. The damaged area of the B2 column calculated by the combined forecasting model

Table 7: Statistics of evaluation index parameters calculated by different models in training sets.

Training set	Sample number	IOWA		IOWGA		IOWHA	
		E_C (%)	V_C	E_C (%)	V_C	E_C (%)	V_C
I_5	5	96.9	0.00140	85.6	0.01300	82.2	0.01800
I_6	6	97.2	0.00100	85.3	0.01200	82.4	0.01500
I_7	7	97.3	0.00083	85.0	0.01000	82.5	0.01300
I_8	8	97.4	0.00067	84.8	0.00870	82.7	0.01100
I_9	9	97.5	0.00055	84.6	0.00740	82.8	0.00920
I_{10}	10	97.5	0.00046	84.5	0.00620	83.0	0.00770
I_{11}	11	97.6	0.00038	84.4	0.00510	83.2	0.00620
I_{12}	12	97.7	0.00031	84.3	0.00420	83.4	0.00500
I_{13}	13	97.7	0.00025	84.3	0.00330	83.6	0.00380
I_{14}	14	97.8	0.00019	84.2	0.00250	83.8	0.00280
I_{15}	15	97.8	0.00015	84.3	0.00180	83.9	0.00200
I_{16}	16	97.9	0.00009	84.3	0.00110	84.1	0.00120
I_{17}	17	98.0	0.00005	84.4	0.00057	84.4	0.00059

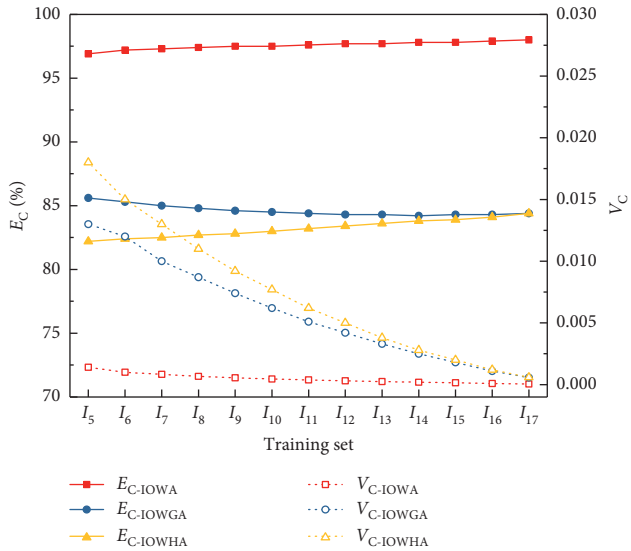

Figure 13: Curves of E_C and V_C of training sets.

Table 8: Statistics of evaluation index parameters calculated by different models in testing sets.

Testing set	Sample number	IOWA		IOWGA		IOWHA	
		E_C (%)	V_C	E_C (%)	V_C	E_C (%)	V_C
$\overline{I}_5$	13	98.5	0.00045	87.0	0.00310	85.4	0.00270
$\overline{I}_6$	12	98.4	0.00048	86.1	0.00250	84.9	0.00210
$\overline{I}_7$	11	98.2	0.00057	85.4	0.00210	84.5	0.00180
$\overline{I}_8$	10	98.0	0.00071	84.7	0.00200	84.0	0.00170
$\overline{I}_9$	9	97.7	0.00089	84.1	0.00220	83.7	0.00200
$\overline{I}_{10}$	8	97.4	0.00120	83.5	0.00260	83.3	0.00270
$\overline{I}_{11}$	7	97.0	0.00150	82.9	0.00360	82.9	0.00380
$\overline{I}_{12}$	6	96.6	0.00220	82.4	0.00510	82.5	0.00550
$\overline{I}_{13}$	5	96.0	0.00330	81.7	0.00750	81.9	0.00800
$\overline{I}_{14}$	4	95.1	0.00550	80.9	0.01100	81.1	0.01200
$\overline{I}_{15}$	3	0.936	0.01100	0.796	0.01800	0.799	0.01800
$\overline{I}_{16}$	2	0.901	0.02600	0.772	0.02900	0.775	0.03000
$\overline{I}_{17}$	1	0.813	0.07900	0.737	0.08000	0.739	0.08100

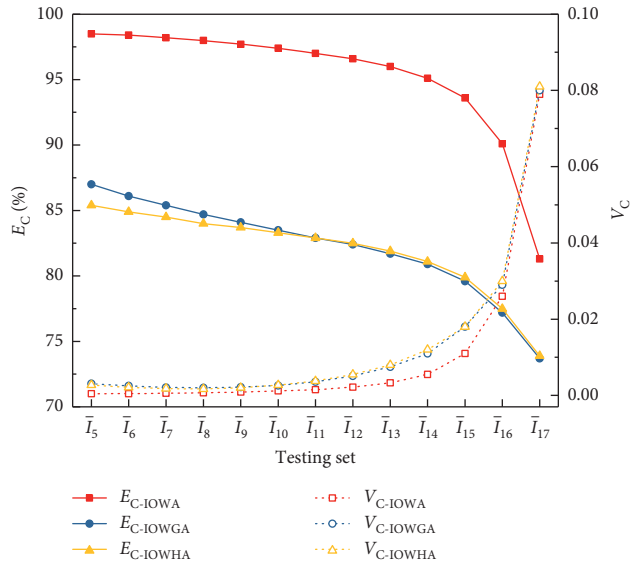

Figure 14: Curves of E_C and V_C of testing sets.

(a) (b) (c)

Figure 15: Nondestructive tests of the B2 column: (a) Double-Cirold Longevity Pavilion; (b) stress wave; (c) drilling resistance.

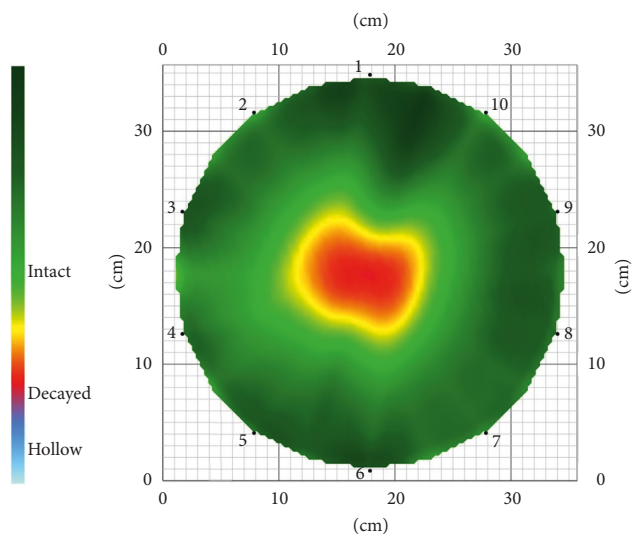

(a)

Figure 16: Continued.

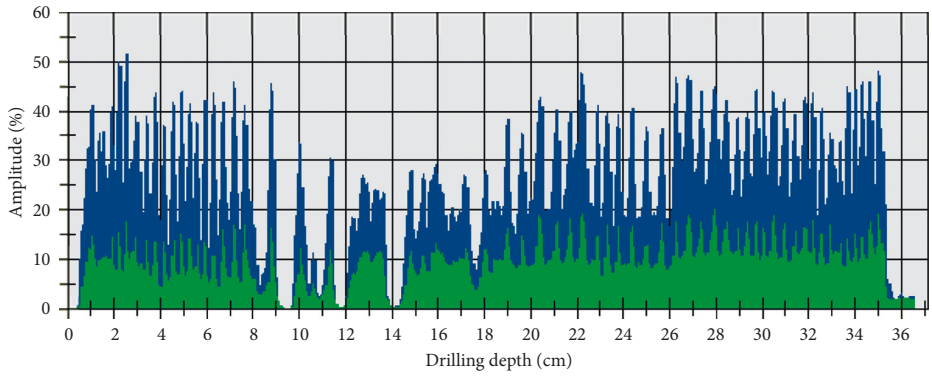

(b)

Figure 16: Detection image: (a) stress wave detection; (b) drilling resistance detection.

based on the IOWA operator is 87.47 cm^2. It is found that the B2 column is defective and the wooden column needs to be repaired.

7. Conclusion

(1) When used alone, both the stress wave and drilling resistance tests have their own advantages and disadvantages. Through analysis, it is found that the stress wave image and the resistance curve have good correspondence in this test, which can make up for their respective shortcomings. Stress wave and drilling resistance tests can be used together to qualitatively analyze the internal damage of the wood structure.

(2) Weighing test results of the stress wave and drilling resistance and establishing a combined forecasting model can quantify the test results. Compared with the combined forecasting models based on the entropy value and Shapley value, the combined forecasting models based on the IOWA operator, IOWGA operator, and IOWHA operator have better forecasting effects according to the idea of variable weight, not only greatly reducing the sensitivity of the results to poor detection methods but also effectively improving the forecasting precision of internal damage of timber components in ancient buildings. When the internal damage of the wood specimen is small, the method proposed in this paper is more effective in improving the precision of stress wave detection.

(3) The mean precision and mean absolute error calculated by the combined forecasting model based on the IOWA operator are 91.7% and 3.42 cm^2. The mean precision is improved by 25.8% and 4.7% compared to the stress wave and drilling resistance tests. In addition, C_{IOWA} is 97.2%, and the overall forecasting effect of the combined forecasting model based on the IOWA operator is the best of all. The analysis results based on the cross-validation theory show that the combined forecasting model based on the IOWA operator has the optimal performance and good applicability. The model can quickly and accurately analyze and judge the internal damage of timber components in ancient buildings qualitatively and quantitatively.

Data Availability

The data used to support the findings of this study are available from the corresponding author upon request.

Conflicts of Interest

The authors declare that they have no conflicts of interest.

Acknowledgments

This study was financially supported by the National Key R&D Program of China (grant no. 2018YFD1100902-01), the National Natural Science Foundation of China (grant nos. 51678017 and 51678005), Beijing Municipal Education Commission Science and Technology General Project (grant no. KM201810005021), Beijing Natural Science Foundation Project (8182008), and the Open Fund of Shanghai Key Laboratory of Engineering Structure Safety (no. 2017-KF03).

References

[1] C. Calderoni, G. De Matteis, C. Giubileo, and F. M. Mazzolani, "Experimental correlations between destructive and non-destructive tests on ancient timber elements," *Engineering Structures*, vol. 32, no. 2, pp. 442–448, 2010.

[2] M. Riggio, R. W. Anthony, F. Augelli et al., "In situ assessment of structural timber using non-destructive techniques," *Materials and Structures*, vol. 47, no. 5, pp. 749–766, 2014.

[3] S. Rust and L. Göcke, "A new tomographic device for the non-destructive testing of standing tree," in *Proceedings of the 12th International Symposium on Nondestructive Testing of Wood: University of Western Hungary*, Sopron, Hungary, September 2000.

[4] X. Li, J. Dai, W. Qian, and L.-H. Chang, "Prediction of internal defect area in wooden components by stress wave velocity analysis," *Bioresources*, vol. 10, no. 3, pp. 4167–4177, 2015.

[5] U. Dackermann, K. Crews, B. Kasal et al., "In situ assessment of structural timber using stress-wave measurements," *Materials and Structures*, vol. 47, no. 5, pp. 787–803, 2014.

[6] T. Lechner, Y. Sandin, and R. Kliger, "Assessment of density in timber using X-Ray equipment," *International Journal of Architectural Heritage*, vol. 7, no. 4, pp. 416–433, 2013.

[7] S. Franke, B. Franke, and F. Scharmacher, "Assessment of timber structures using the X-ray technology," in *Procedings of the 2nd International Conference on Structural Health Assessment of Timber Structures (SHATIS 2013)*, Trento, Italy, September 2013.

[8] M. Riggio, J. Sandak, and S. Franke, "Application of imaging techniques for detection of defects, damage and decay in timber structures on-site," *Construction and Building Materials*, vol. 101, no. 2, pp. 1241–1252, 2015.

[9] F. Isik and B. Li, "Rapid assessment of wood density of live trees using the resistograph for selection in tree improvement programs," *Canadian Journal of Forest Research*, vol. 33, no. 12, pp. 2426–2435, 2003.

[10] B. Kasal and R. W. Anthony, "Advances inin situ evaluation of timber structures," *Progress in Structural Engineering and Materials*, vol. 6, no. 2, pp. 94–103, 2004.

[11] T. P. Nowak, J. Jasieńko, and K. Hamrol-Bielecka, "In situ assessment of structural timber using the resistance drilling method—evaluation of usefulness," *Construction and Building Materials*, vol. 102, no. 1, pp. 403–415, 2016.

[12] L. Espinosa, F. Prieto, L. Brancheriau, and P. Lasaygues, "Effect of wood anisotropy in ultrasonic wave propagation: a ray-tracing approach," *Ultrasonics*, vol. 91, pp. 242–251, 2019.

[13] D. A. Gatto, M. R. F. Goncalves, B. D. Mattos, L. Calegari, and D. M. Stangerlin, "Estimativa da deterioração da madeira de assoalho de prédio histórico por meio de ondas ultrassônicas," *Cerne*, vol. 18, no. 4, pp. 651–656, 2012.

[14] K. J. Vössing, M. Gaal, and E. Niederleithinger, "Air-coupled ferroelectret ultrasonic transducers for nondestructive testing of wood-based materials," *Wood Science and Technology*, vol. 52, no. 6, pp. 1527–1538, 2018.

[15] X. Q. Yue, L. H. Wang, A. P. Wacker, and Z. M. Zhu, "Electric resistance tomography and stress wave tomography for decay detection in trees-a comparison study," *PeerJ*, vol. 7, article e6444, 2019.

[16] Z. X. Liu, X. H. Di, L. H. Wang, and T. Y. Sun, "Effect of different detection angle on propagation velocity of stress wave in health standing trees," *Journal of North-East Forestry University*, vol. 42, no. 4, pp. 105–108, 2014.

[17] X. Guan, M.-C. Zhao, Z. Wang, W.-L. Sha, and Z.-R. Zhou, "Study of stress wave speed and elastic modulus measurement of poplar log base on longitudinal resonance," *Journal of West China Forestry Science*, vol. 42, no. 2, pp. 14–19, 2013.

[18] G. Li, X. Weng, X. Du, X. Wang, and H. Feng, "Stress wave velocity patterns in the longitudinal-radial plane of trees for defect diagnosis," *Computers and Electronics in Agriculture*, vol. 124, pp. 23–28, 2016.

[19] E. Guntekin, Z. G. Emiroglu, and T. Yilmaz, "Prediction of bending properties for Turkish red pine (*Pinus brutia* Ten.) lumber using stress wave method," *Bioresources*, vol. 8, no. 1, pp. 231–237, 2013.

[20] T. Y. Sun and L. H. Wang, "Non-destructive testing of log internal decay based on two-dimensional CT images of stress wave and X-ray testing," *Forest Engineering*, vol. 27, no. 6, pp. 26–29, 2011.

[21] Q. Wei, B. Leblon, and A. La Rocque, "On the use of X-ray computed tomography for determining wood properties: a review1This article is a contribution to the series the role of sensors in the new forest products industry and bioeconomy," *Canadian Journal of Forest Research*, vol. 41, no. 11, pp. 2120–2140, 2011.

[22] L. P. Perlin, Â. D. Valle, and R. C. de Andrade Pinto, "New method to locate the pith position in a wood cross-section based on ultrasonic measurements," *Construction and Building Materials*, vol. 169, pp. 733–739, 2018.

[23] T.-Y. Yu, B. Boyaci, and H. F. Wu, "Simulated transient electromagnetic response for the inspection of GFRP-wrapped concrete cylinders using radar NDE," *Research in Nondestructive Evaluation*, vol. 24, no. 3, pp. 125–153, 2013.

[24] L. H. Chang, W. Qian, and J. Dai, "Combination forecasting research on timber building internal defects," *Journal of Simulation Systems, Science and Technology*, vol. 17, no. 25, pp. 1473–8031, 2016.

[25] Y. An, Y. F. Yin, X. M. Jiang, and Y. C. Zhou, "Inspection of decay distribution in wood column by stress wave and resistograph techniques," *Journal of Building Materials*, vol. 11, no. 4, pp. 457–463, 2008.

[26] L. H. Chang, X. H. Chang, H. Chnag, W. Qian, L. T. Cheng, and X. L. Han, "Nondestructive testing on ancient wooden components based on Shapley value," *Advances in Materials Science and Engineering*, vol. 2019, Article ID 8039734, 11 pages, 2019.

[27] W. Qian, J. Dai, X. Li, and L. H. Chang, "The systematic application of non-destructive testing techniques for ancient wood buildings," in *Proceedings of the 4th International Conference on Civil Engineering and Building Materials (CEBM)*, Hong Kong, China, November 2014.

[28] X. W. Ge, L. H. Wang, T. Y. Sun et al., "Quantitative detection of salix matsudana inner decay based on stress wave and resistograph techniques," *China Forestry Science and Technology*, vol. 28, no. 5, pp. 87–91, 2014.

[29] X. P. Wang and R. B. Allison, "Decay detection in red oak trees using a combination of visual inspection, acoustic testing, and resistance microdrilling," *Arboriculture & Urban Forestry*, vol. 34, no. 1, pp. 1–4, 2008.

[30] S.-T. Chuang and S.-Y. Wang, "Evaluation of standing tree quality of Japanese cedar grown with different spacing using stress-wave and ultrasonic-wave methods," *Journal of Wood Science*, vol. 47, no. 4, pp. 245–253, 2001.

[31] C. Rabe, D. Ferner, S. Fink, and F. W. M. R. Schwarze, "Detection of decay in trees with stress waves and interpretation of acoustic tomograms," *Arboricultural Journal*, vol. 28, no. 1-2, pp. 3–19, 2004.

[32] J. M. Bates and C. W. J. Granger, "The combination of forecasts," *OR*, vol. 20, no. 4, pp. 451–468, 1969.

[33] R. R. Yager, "Induced aggregation operators," *Fuzzy Sets and Systems*, vol. 137, no. 1, pp. 59–69, 2003.

[34] H. Y. Chen and C. L. Liu, "A kind of combination forecasting method baesd on induced ordered weighted averaging (IOWA) operators," *Forecasting*, vol. 22, no. 6, pp. 61–65, 2003.

[35] M. Aggarwal, "A new family of induced OWA operators," *International Journal of Intelligent Systems*, vol. 30, no. 2, pp. 170–205, 2015.

[36] H. Y. Chen and Z. H. Sheng, "A kind of new combination forecasting method based on induced ordered weighted geometric averaging (IOWGA) operator," *Journal of Industrial Engineering and Engineering Management*, vol. 19, no. 4, pp. 36–39, 2005.

[37] J. W. Yang, D. S. Shao, Z. M. Wang et al., "A new method of variable weight combination forecasting based on entropy

weight and IOWGA operator," *Journal of Geodesy and Geodynamics*, vol. 37, no. 12, pp. 1243–1247, 2017.

[38] H. Y. Chen, C. L. Liu, and Z. H. Sheng, "Induced ordered weighted harmonic averaging (IOWHA) operator and its application to combination forecasting method," *Chinese Journal of Management Science*, vol. 12, no. 5, pp. 35–40, 2004.

[39] J. Z. Zhao, T. X. Xu, H. J. Li, and W. Ye, "Consumption forecast of missile spare parts based on improved theil coefficient," *Systems Engineering & Electronics*, vol. 35, no. 8, pp. 1681–1686, 2013.

[40] H. Li, D. Chen, E. Arzaghi et al., "Safety assessment of hydrogenerating units using experiments and grey-entropy correlation analysis," *Energy*, vol. 165, pp. 222–234, 2018.

[41] S. Huang, B. Ming, Q. Huang, G. Leng, and B. Hou, "A case study on a combination NDVI forecasting model based on the entropy weight method," *Water Resources Management*, vol. 31, no. 11, pp. 3667–3681, 2017.

[42] L. H. Chang, J. Dai, and W. Qian, "Nondestructive testing of internal defect of ancient architecture wood members based on Shapley value," *Journal of Beijing University of Technology*, vol. 42, no. 6, pp. 886–892, 2016.

[43] Y. Tang, Q. Xu, B. Ke et al., "Study on optimization of SVM model of rock blasting fragmentation based on cross-validation," *Blasting*, vol. 35, no. 3, pp. 74–79, 2018.

[44] F. G. R. de Oliveira, M. Candian, F. F. Lucchette, J. Luis Salgon, and A. Sales, "A technical note on the relationship between ultrasonic velocity and moisture content of Brazilian hardwood (*Goupia glabra*)," *Building and Environment*, vol. 40, no. 2, pp. 297–300, 2005.

[45] H. Liu and J. M. Gao, "Effects of moisture content and density on the stress wave velocity in wood," *Journal of Beijing Forestry University*, vol. 36, no. 6, pp. 154–158, 2014.

[46] MOHURD GB/T.50329-2012, "Standard for design of timber structures," Tech. Rep., China Architecture Building Press, Beijing, China, 2017.

[47] MOHURD GB/T.50329-2012, "Standard for test methods of timber structures," Tech. Rep., China Architecture Building Press, Beijing, China, 2012.

[48] J. Jasienko, T. Nowak, and K. Hamrol, "Selected methods of diagnosis of historic timber structures-principles and possibilities of assessment," in *Proceedings of the 2nd International Conference on Structural Health Assessment of Timber Structures (SHATIS)*, Trento, Italy, September 2014.

[49] J. M. Branco, M. Piazza, and P. J. S. Cruz, "Structural analysis of two king-post timber trusses: non-destructive evaluation and load-carrying tests," *Construction and Building Materials*, vol. 24, no. 3, pp. 371–383, 2010.

[50] R. R. Yager, "Family of OWA operators," *Fuzzy Sets and Systems*, vol. 59, no. 2, pp. 125–148, 1993.

[51] Z. S. Xu and Q. L. Da, "The ordered weighted geometric averaging operators," *International Journal of Intelligent Systems*, vol. 17, no. 7, pp. 709–716, 2002.